Durham Research Online

A Comparative Analysis of Global Shape Analysis Methods for the Assessment of the Human Right Ventricle

Jia Wu[a], Marc A. Simon[b,c], John C. Brigham[c,d,*]

[a1]*Department of Radiology, University of Pennsylvania, Philadelphia, PA, 19104 USA*
[b]*Cardiovascular Institute, School of Medicine, University of Pittsburgh, Pittsburgh, PA, 15261 USA*
[c]*Department of Bioengineering , University of Pittsburgh, Pittsburgh, PA, 15219 USA*
[d]*Department of Civil and Environmental Engineering, University of Pittsburgh, Pittsburgh, PA, 15261 USA*

Abstract

Two contemporary statistical shape analysis workflows are presented and compared with respect to analysis of the human right ventricle (RV). The methods examined include an approach that directly applies proper orthogonal decomposition to harmonically mapped surfaces (DM-POD) and an approach that expands the harmonically mapped surfaces onto spherical harmonic functions prior to further analysis (SPHARM). The structure of both workflows is elaborated upon and compared, particularly regarding the details of several key sub-steps, including the shape parameterization, alignment, and statistical decomposition. The performance is evaluated for the components of each framework at the various analysis stages, as well as for the output of the complete workflows in terms of the potential to assess right ventricular function through application to a set of RV endocardial surfaces with varying levels of pulmonary hypertension. Additionally, DM-POD and SPHARM are examined with respect to different methods of utilizing the available phases captured throughout a single cardiac cycle for the patient set. The DM-POD workflow is quantitatively shown to provide more anatomically consistent representations of the RV, while in general, the features produced by the two workflows are shown to be distinctly different. Furthermore, both the workflow components and the components (i.e., phases) of

---

*Tel.: +1 412 624 9047; fax: +1 412 624 0135. E-mail address: brigham@pitt.edu

the cardiac cycle utilized for the shape analysis are quantitatively shown to significantly affect the pattern analysis of the patient set.

1. Introduction

1.1. Clinical Motivation

Cardiac remodeling plays a crucial role in the progression of heart disease and the outcome of therapies, and therefore, both the static and functioning appearance of the human heart are thought to provide substantial diagnostic information relating to any number of cardiovascular diseases [1]. While a considerable amount of work over the years has focused on the function of the left ventricle (LV) and its relation to several diseases [2], recent focus has extended to the right ventricle (RV) as studies have shown a more significant dependance than previously thought of cardiac health on RV function for certain diseases, such as pulmonary hypertension (PH) [3] and Tetralogy of Fallot (TOF) [4]. For instance, PH is a cardio-pulmonary disease with a wide variety of causes, and therefore treatments, but left untreated PH invariably alters the size and shape of the RV [3]. Typically, the RV subject to PH dilates with a variable amount of increased wall thickness or hypertrophy. Yet, even though untreated PH can be a devastating disease with poor long-term prognosis (particularly the subset of patients with pulmonary arterial hypertension, in which the cardiopulmonary abnormality is in the pulmonary arterial vascular bed), diagnosis is often delayed because the early symptoms of PH are nonspecific [5]. Additional delay in diagnosis and/or treatment can result from the limited understanding and available metrics of RV shape and related functional changes to predict the level of deterioration in heart function [3]. The RV poses a particular challenge for identifying such metrics, as the RV anatomy is naturally complex, varies significantly both during the cardiac cycle and across patient populations, and often becomes even more complicated with disease. As such, creating sufficient analysis tools for developing a better clinical understanding of right heart function has generally remained a significant open challenge to-date [6].

1.2. Technical Background

Developments in medical imaging techniques and computer-aided diagnosis (CAD) have made significant contributions to aid physicians in both

observing the nature of disease-related shape changes in biological structures and identifying diagnostic relationships between a shape change and a particular pathology [7]. Statistical shape analysis (in some instances interchangeably referred to as geometric morphometrics) is one particular CAD approach that has been shown to provide promising results for certain applications [8, 9, 10, 11]. Generally, statistical shape analysis obtains shape-based representations of a biological structure of interest from available medical images and then performs statistical analysis on a collection of these representations to study the geometrical or kinematic variations. Common aims of statistical shape analysis are to extract metrics from the given set of medical images for diagnostic purposes [12, 13, 14, 15, 16] or to obtain fundamental features to aid with future image processing [17]. In terms of applications to understanding and diagnosing pathology, statistical shape analysis methods to-date have been largely focused on components of the brain and heart and their associated afflictions. Such applications have included analyzing changes in the shape of the hippocampus and/or the ventricles of the brain with respect to Alzheimer's disease [18, 19] and Schizophrenia [12, 13] and analyzing changes in the shape of the RV with respect to PH [16] and TOF [14, 15].

A typical statistical shape analysis framework includes several common steps, with the first being to preprocess the image sets. Preprocessing includes some combination (not necessarily in this order or including all steps) of segmentation, establishing base mathematical representations of the shapes, alignment/registration, and parameterization, which is the critical (and often most challenging) step in building the necessary correspondence between the collection of medical shapes [20]. Once a final correspondence is set, standard pattern recognition methods can be applied to derive the fundamental shape features that exist within the shape sets, commonly utilizing some variant of principle component analysis (PCA) [14, 16], and then generate metrics and classifiers associated with the function and/or pathology of the application of interest.

There have been a wide variety of specific techniques employed within statistical shape analysis frameworks depending on specific features, restrictions, and/or objectives of the particular applications that have been considered. With respect to the base representation of shape, one straightforward concept that has been used is to define the collection of surface points describing the shape in a standard Cartesian coordinate system, either in a discrete or continuous format. For discrete descriptions, a popular method has been

to use anatomical features as landmarks or fiducial points to represent the geometric features among a population [8, 21]. However, due to limitations on the availability of landmarks in many applications, other more mathematically based methods have been introduced to automatically generate dense collections of semi-landmarks (i.e., surface points not necessarily related to anatomical features) to represent the shape, with point distribution models being a popular method within this category [22]. For continuous descriptions, mesh-based techniques (e.g., point distributions interpolated with polynomials with compact support) are a common means for shape representation [23]. Alternatively, global basis functions (i.e., functions with non-compact support) have also been utilized for representation of shape, including basis functions such as spherical harmonic functions (SPHARM) [24] or wavelet functions [25]. Lastly, skeletonization approaches have been used in some applications for the shape representation, such as the medial shape description, which defines the shape in terms of a medial axis and the radial distance from this medial axis to the shapes surface [26]. Some of these approaches for quantitatively describing the shape are automatically comparable in a logical and anatomically consistent manner, such as the methods that simply rely on a set of anatomical features/landmarks. However, more generally, and particularly when anatomical landmarks are limited, further processing is required to build correspondence (i.e., a one-to-one relationship between each point describing each shape). One common technique has been to utilize some form of topological mapping to map every point on each shapes surface through some consistent mathematical technique (e.g., simple projection [20] or harmonic mapping [27]) to a common topologically equivalent structure, such as the surface of a plate or a sphere [20]. Finally, rigid registration is often applied to remove effects of size, orientation, and/or position, so that the subsequent statistical analysis can be focused on shape alone. The shapes can be aligned simply in some cases through manual manipulation or casting the statistical analysis in terms of the difference in shape from a reference position/shape [28]. Alternatively, some applications require more elaborate registration algorithms, such as methods that define a template shape and align each shape by minimizing the distance to the template through the iterative closest point algorithm [29] or the procrustes methodology [30], or some of the SPHARM approaches, which actually utilize components of the base shape representation itself (e.g., the first-order ellipsoidal component) to align each shape [22]. Again, a critical point is that in some instances the specific statistical shape analysis implementation

4

is chosen based on requirements/limitations of the specific application and available resources, such as limited computational capability or insufficient available fiducial points. However, in many other cases there is not necessarily any restrictions forcing the use of a specific approach, and yet the nature of the application (i.e., the organ/structure and disease of interest) should dictate the use of one methodology over another.

Cardiac structures represent one area of significant interest for statistical shape analysis methods, as cardiac dysfunction is often thought to be measurable through distortion within the geometric features at a specific cardiac phase or by deterioration/changes in the kinematic patterns within the cardiac cycle [31, 6]. However, cardiac structures represent a particular challenge also, in comparison to many other clinical applications to-date. These challenges are largely due to the substantial shape variability that can be seen across a population and resulting from various pathological changes, as well as the dynamic variations in shape seen throughout the cardiac cycle. The concept of statistical shape analysis for cardiac structures was first introduced in [32], which used a landmark-based representation of the LVs and RVs at end-diastole (ED) and derived shape features from these with PCA. Since the work of Frangi et al., there have been a variety of other techniques applied to cardiac structures in a variety of ways (e.g., utilizing varying heart components, landmarks, and/or phases in the cardiac cycle). For instance, Huang et al. used SPHARM descriptors along with alignment techniques based on the spherical harmonic decomposition to examine the shape of the endocardial and epicardial surfaces of LVs throughout a cardiac cycle, and then heuristically derived features of these shapes and used hierarchical clustering methods to examine mechanical dyssynchrony of the heart [33]. Andreopoulos and Tsotsos presented a framework that also used landmark-based models for the endocardial and epicardial surfaces of LVs throughout a cardiac cycle, and combined PCA to produce active shape and appearance models to be used for automated segmentation purposes [34]. Similarly, Zhang et al. used landmark-based models within a combination active shape and appearance model using PCA for the endocardial and epicardial surfaces of LVs and RVs throughout a cardiac cycle to first aid with segmentation, and then to build quantitative shape, motion, and volumetric features for classification of TOF [15] Alternatively, Mansi et al. introduced currents and diffeomorphic registration algorithms to build correspondence for mesh-based continuous descriptions of RV endocardial surfaces at ED, then PCA was applied to reduce the dimensionality as well as derive quanti-

tative features to identify correlations with the clinical metrics and to better classify and understand TOF [14]. Recently, Wu et al. also used mesh-based continuous descriptions of RV endocardial surfaces throughout a cardiac cycle, applied a harmonic mapping method and converted the surfaces into relative shape change functions to build correspondences, and then applied proper orthogonal decomposition (POD) (i.e., a continuous form of PCA) to derive kinematic features and build metrics for potential classification of PH [16]. Overall, these recent research efforts in statistical shape analysis applied to the heart have shown promising results for both image processing and pathology classification. However, the recent efforts have also included a diverse set of components in the analysis process (e.g., different mathematical representations, different registration and decomposition techniques, etc.) with limited motivation for why one approach is utilized over another. As stated previously, after factoring out restrictions necessitated by the nature of the available imaging data, a natural assumption is that one computational approach, including both the analysis methods (e.g., representation, decomposition, etc.) and the cardiac information utilized (e.g., specific cardiac phase), will be best suited for a given structure and/or pathology. Yet, minimal work has made comparisons to quantify the effectiveness of alternate shape analysis approaches for a given application.

1.3. Contribution of Study

The present study aims to compare and contrast some approaches to statistical shape analysis that have been utilized to-date for various studies, applied herein to analyze right ventricle endocardial surfaces (RVES) for hearts with and without PH. The investigation focuses on two specific workflows for statistical shape analysis, a spherical harmonic function-based approach, as presented in [22], and a direct decomposition approach, as presented in [16], comparing the components of each framework at the various analysis stages (representation, alignment, decomposition) as well as the output of the complete workflows in terms of the potential to assess RV function. Additionally, different methods of utilizing the available imaging data are also investigated by considering analysis results when incorporating several different combinations of the phases captured throughout a single cardiac cycle for the patient set. As such, the present study is intended to:

(1) - explore through comparison the efficiency and effectiveness of these specific shape preprocessing and feature extraction approaches applied

to the human RV with respect to PH, and provide guidance on techniques to use for further (larger) studies of the same or similar biological structure and pathology.

(2) - generally provide an example structure of the tests that could, and in many cases should be performed toward determining the most suitable shape analysis strategy for a given pathology and/or biological structure of interest.

It should be noted that the unique set of imaging and clinical information utilized were available for a total of only 13 patients for this study. However, each patient had 9 distinct timeframes (so, totaling 117 image sets), which could be considered sufficient for a detailed method comparison, as is presented herein. Moreover, it is not the intention of this study to generate a statistically significant pathologically-relevant conclusion at this time.

The following section presents the specifics of the components for the two statistical shape analysis workflows considered herein. In Section 3 the statistical shape analysis components and the complete workflows are examined with respect to analysis of a clinically obtained set of RVES, which is followed by concluding remarks in Section 4.

2. Methods

Two different contemporary statistical shape analysis approaches were chosen to be applied to assess human RV function and compared for the present study: (1) an approach that directly applies POD to harmonically mapped surfaces, as shown in [16], and (2) an approach that also harmonically maps the surfaces, but then projects the surfaces onto spherical harmonic functions prior to further analysis, as shown in [35]. In addition, the analysis and assessment of each approach included two different alignment techniques for comparison purposes. In the remaining text the direct mapping to POD approach will be referred to as the DM-POD approach and the spherical harmonic function-based approach will be referred to simply as the SPHARM approach. An overview of the analysis approaches considered herein is shown in Fig. 1. In brief, both approaches begin with segmenting 3D surface representations of the RVES from the cardiac image sets and generating mesh-based representations of the surfaces. Then, the respective version of harmonic mapping is applied to parameterize the set of RVES with
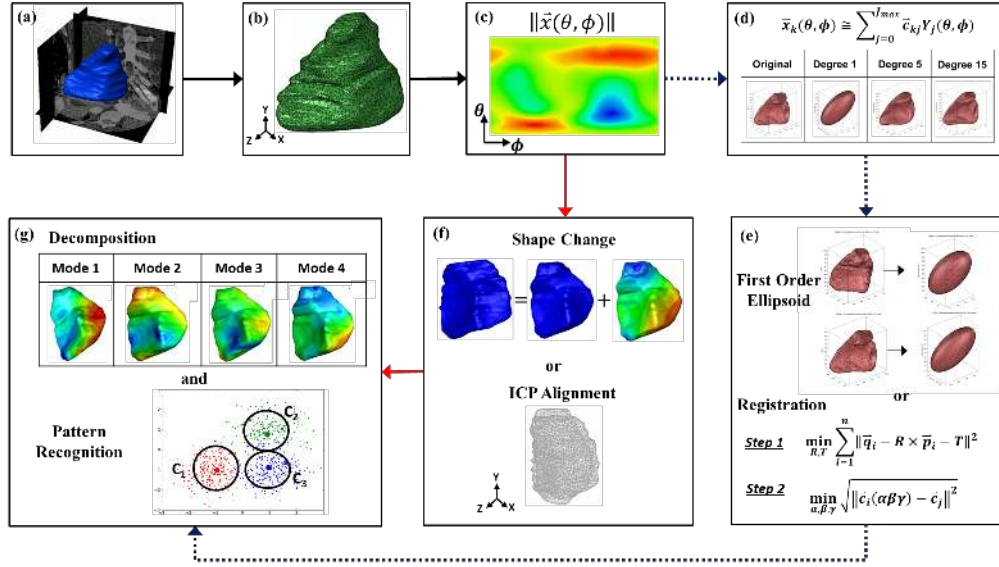
Figure 1: Schematic of the statistical shape analysis workflows, including the approach that directly applies POD to harmonically mapped surfaces (DM-POD - solid red arrows) and the approach that projects the surfaces onto spherical harmonic functions after harmonic mapping (SPHARM - dotted blue arrows), showing the key steps of (a) segmentation of the right ventricle endocardial surface (RVES) from the medical images, (b) smoothing and interpolated 3D closed surface mesh generation, (c) parameterization of the RVES in terms of spherical coordinates (shown in 2D), (d) projection of the RVES onto a spherical harmonic function basis (SPHARM), (e) alignment of the surfaces based on the spherical harmonic function parameterization (SPHARM), (f) alignment of the surfaces either by conversion into shape change functions or by a rigid registration algorithm (DM-POD), and (g) decomposition of the shape sets into modes and application of pattern recognition techniques.

respect to a common domain. As shown with the solid red line in Fig. 1, the DM-POD approach goes directly from harmonic mapping to alignment of the shapes by either converting the shapes into relative shape change functions over the cardiac cycle of each patient or registering the shapes to a preselected shape template. Once the set is aligned, the DM-POD approach applies POD to decompose the set of shapes or shape change functions into modes, and pattern recognition techniques are utilized to generate features from the modes, cluster the population, and/or build classifiers. Alternatively, as shown with the dotted blue line in Fig. 1, following harmonic mapping the SPHARM approach redefines the shapes in terms of a spherical harmonic function basis. Then, the SPHARM approach aligns the shapes either based on the orientation of the first-order ellipsoidal basis function or using a combination of template registration and an approach that rotates the surfaces in the space of the spherical harmonic coefficients. Lastly, the SPHARM approach utilizes PCA to decompose the sets of coefficients of the spherical harmonic functions to similarly obtain shape modal vectors (in the space of the spherical harmonic basis), and then pattern recognition techniques are applied. Note that PCA and POD can be considered conceptually identical, but are differentiated here such that POD is applied to decompose the continuous descriptions and PCA is applied to decompose the discrete descriptions. In the following, each step of the analysis methods, including the surface representation, parameterization, registration, and statistical decomposition, are elaborated upon.

2.1. Image Acquisition and Surface Extraction

The present work utilized a clinically obtained set of ECG-gated multi-slice cardiac CT images corresponding to 13 separate patients from a study on regional RV structural and functional adaptation to PH as previously reported in [36]. The 3D surface descriptions of the RV shapes were obtained for each of the 9 unique phases captured from the cardiac cycle for each of the 13 patients by manually segmenting the RVES from each image in the CT stacks, interpolating the slices, and then smoothing the interpolated surfaces using a standard recursive and discrete Gaussian filter within the commercial medical image processing software Simpleware [1]. Thus, each of the 3D surfaces could be considered as a continuous, linearly interpolated, mesh-based

---

[1]www.simpleware.com

representation, and the collection of 117 (13 patients with 9 cardiac phases per patient) continuous, 3D, non-overlapping, closed, genus-0 RVES are labeled as $\{\Omega_k\}_{k=1}^{117}$. Manual segmentation was used to ensure that the most anatomically accurate representations of the ventricle shape were segmented within the constraints of the CT image quality. Similarly, the endocardial surface was chosen specifically due to the relatively high imaging contrast between the wall tissue and contrast-enhanced blood. The segmentation was overseen and verified by a trained cardiologist (M. A. Simon), who has over ten years of experience in advanced heart failure, PH, and in particular, experience in the imaging of the RV.

2.2. Surface Parameterization

Both approaches initially utilized a harmonic topological mapping method, so that the RVES were quantitatively comparable over a common domain for further analysis. A harmonic mapping (i.e., change in coordinates) is simply a parameterization that satisfies Laplace's equation for each new parameter ([37]). As such, choosing the new parameters to be the spherical coordinates, ϕ (longitude) and θ (latitude), the spherical coordinates for each point on the kth RVES (i.e., location of the RVES coordinates on the unit sphere) can be determined from the solution of

$$\nabla^2 \theta(\vec{x}) = 0 \text{ and } \nabla^2 \phi(\vec{x}) = 0, \ \forall \vec{x} \in \Omega_k. \tag{1}$$

Provided with sufficient boundary conditions for θ and ϕ, which will be discussed in more detail in the following, Eqn. 1 can be numerically solved, and then each RVES can be described over the common domain as

$$\vec{x} = \vec{x}(\theta, \phi) \text{ in } \theta \in [0, \pi], \phi \in [0, 2\pi], \ \forall \vec{x} \in \Omega_k. \tag{2}$$

2.2.1. DM-POD Approach:

For the DM-POD approach, each surface mesh was parameterized solely using a two step variation of harmonic topological mapping. Specifically, the DM-POD approach creates an initial mapping by solving Eqn. 1 with boundary conditions for θ and ϕ corresponding to anatomical features. Accurately determining sufficient anatomical references may be a challenge in certain applications, and yet, by choosing the boundary conditions to relate to specific consistently identifiable anatomical features, this approach is able to maintain anatomical consistency in the parameterization across populations. The RVES data used here provided more than sufficient anatomical

references that could be consistently identified. For the analysis presented the boundary conditions utilized included the apex, where $\theta = 0$, the intersection of the pulmonary valve with the anterior border between the free wall and septum, where $\theta = \pi$, and the entire anterior border between the free wall and septum, where ϕ has a non-unique value of 0 and 2π. A secondary parameterization is then applied due to the fact that using only the initial harmonic mapping may lead to the surface information being excessively concentrated in the mapped domain with a majority of the surface having initial ϕ and/or θ values within a relatively small range, which may cause numerical difficulties and degrade the subsequent analysis. This second step relies on the observation that the harmonic parameterization of a sphere defines the relationship between uniformly distributed spherical surface coordinates over the unit sphere domain (the same domain as the mapped domain) and the distortion caused by the mapping, and therefore the inverse of this mapping, which is what is utilized, will "undo" some amount of the distortion caused by the harmonic mapping process. See [38] for additional details about the two-step mapping approach used for the DM-POD workflow.

2.2.2. SPHARM Approach:

In contrast to the DM-POD approach, the SPHARM approach considers the surfaces in a discrete format in terms of the mesh vertices and connectivity, and a spherical parameterization algorithm known as the control of area and length distortions (CALD) is applied to perform the mapping ([39]). The CALD algorithm consists of an initial harmonic parameterization followed by local and global smoothing methods. For initial parameterization, the CALD approach does not use anatomical landmarks for the harmonic mapping boundary conditions, as was the case in DM-POD. Rather, CALD identifies two poles ($\theta = 0$ and $\theta = \pi$) to be the two vertices whose projections onto the principal Cartesian axis are furthest apart, then defines a dateline ($\theta = 0$ or $\theta = 2\pi$) as the path with the steepest latitude ascent, and applies these boundary conditions to solve Eqn. 1. Then, in order to improve the area distortion (i.e., the inconsistent ratio between the area of the elements within the original surface mesh and the initial parametrized mesh), the latitude obtained from the initial mapping is re-parameterized twice using a rotation operator, and the best (i.e., the parameterized mesh with minimal overall area distortion) of these three parameterization results (including the initial) is chosen for future usage. To further compensate for the area distortion the CALD approach uses an optimization algorithm that

11

combines local and global smoothing methods to iteratively relocate vertices of the parameterization based on minimizing the area distortion of the surface mesh elements with controlled length distortion, while also trying to equalize the mesh distribution in terms of area over the spherical coordinates. After parameterization, the SPHARM approach expands each of the mapped surfaces into a combination of spherical harmonic functions, such that the kth RVES can be described as

$$\vec{x}_k(\theta, \phi) \approx \sum_{j=1}^{J_{max}} \left[c_{kj}^{(1)} \sin(\theta)\cos(\phi), c_{kj}^{(2)} \sin(\theta)\sin(\phi), c_{kj}^{(3)} \cos(\theta) \right]^T Y_j(\theta, \phi), \quad (3)$$

where $Y_j(\theta, \phi)$ is the jth spherical harmonic basis function, $c_{kj}^{(i)}$ is the ith component of the corresponding 3D coefficient vector for the kth RVES, and J_{max} is the number of spherical harmonic functions included in the description. Therefore, each RVES can be defined uniquely by the set of corresponding spherical harmonic function coefficients. For the remaining sections the vector of all spherical harmonic function coefficients used to describe the kth surface is defined as $\vec{c}_k = \left[c_{k1}^{(1)}, c_{k1}^{(2)}, c_{k1}^{(3)}, c_{k2}^{(1)}, c_{k2}^{(2)}, c_{k2}^{(3)}, ... \right]^T$.

2.3. Surface Alignment

Overall, surface alignment is applied to remove the effects of size, orientation, and/or position, so that the subsequent analyses of the RVES set consider shape alone. Two alignment methods were considered here for each shape analysis workflow. The DM-POD workflow included one approach that converts the shape sets into relative shape change (i.e., pseudo-displacement) functions of the RVES for each patient, and another approach that is a more standard rigid registration approach derived from the iterative closest point algorithm. Alternatively, the SPHARM workflow tested an alignment approach based on the first-order ellipsoidal component of the spherical harmonic function expansion, as well as an approach that minimizes the distance between the shapes in the set with respect to the set of spherical harmonic function coefficients from the expansions.

2.3.1. Pseudo-Displacement:

As shown in [16], an approach to convert RVES shape sets into pseudo-displacement functions has been used to circumvent the additional computational cost and nonuniqueness of traditional registration methods. The primary assumption with this approach is that given a consistently identifiable

phase (i.e., end diastole) to use as reference, the normalized change in shape of an individual's RVES over a cardiac cycle is fundamentally consistently comparable across a population of individuals, provided that any displacement not directly relating to beating of the heart is negligible throughout the image acquisition process. As such, the parameterized RVES can be converted into pseudo-displacement shape change functions simply by subtracting one chosen phase's RVES from each other phase's RVES over the cardiac cycle for each individual separately as

$$\vec{d}_k^i(\theta, \phi) = \vec{x}_k^i(\theta, \phi) - \vec{x}_r^i(\theta, \phi), \quad \text{and} \quad k \neq r, \tag{4}$$

where $\vec{d}_k^i$ is the pseudo-displacement function for the ith patient at the kth timeframe in the cardiac cycle and r is the chosen referential phase index for the corresponding patient. Then, each pseduo-displacement function can be normalized (i.e., scaled) with respect to the maximum change in the cardiac cycle for the corresponding individual as

$$\vec{p}_k^i(\theta, \phi) = \vec{d}_k^i(\theta, \phi)/ \max_j \|\vec{d}_j^i(\theta, \phi)\|_{L_2}, \tag{5}$$

with $\|.\|_{L_2}$ defined as the standard L_2-norm. The end diastole phase was chosen as the referential phase for all analysis herein that used the pseudo-displacement method for alignment.

2.3.2. Iterative Closest Point:

The iterative closest point (ICP) rigid registration algorithm ([40]) was also considered to complete the correspondence for the RVES set within the DM-POD workflow to more directly analyze shape (rather than change in shape). For the ICP algorithm a template surface is chosen from the set, and then each other surface in the set is iteratively rotated and translated until the distance between each surface and the pre-selected template surface is minimized. For the present study, the RVES for an arbitrary non-hypertensive patient at end diastole was chosen as the template shape. Furthermore, only a single final rotation operator and translation vector were determined for each patient using the ICP algorithm in order to align the end diastole RVES of each patient to the template RVES, and then this rotation operator and translation vector were applied to each other phase for each respective patient. Therefore, the kinematic information over the cardiac cycle for each patient was also preserved with this ICP registration approach. In addition,

prior to registration each RVES was normalized, similarly applying a single scaling operator for each patient with respect to the internal cavity volume of the respective end diastole RVES compared to the template surface. Thus, the registered RVES for the ith patient at the kth timeframe in the cardiac cycle can be shown as

$$\vec{p_k^i}(\theta, \phi) = R_{ED}^i \times (S_{ED}^i \times \vec{x}_k^i(\theta, \phi)) + \vec{T}_{ED}^i, \tag{6}$$

where R_{ED}^i, S_{ED}^i, and $\vec{T}_{ED}^i$ are the rotation operator, scaling operator, and translation vector corresponding to the patient at ED phase, respectively.

2.3.3. First-Order Ellipsoid:

The first approach used to address the alignment need in the SPHARM workflow was an approach that relies primarily on the first-order ellipsoidal component of the SPHARM expansion ([22]). For this approach, each RVES is scaled (i.e., normalized) individually with respect to the internal cavity volume (note, this differs from the scaling in the DM-POD workflow, which uses a single scaling value for each patient rather than a separate scaling value for each shape). Next, the 0th-degree spherical harmonic function term is removed from the expansion to center the shapes in the set. The parameterization is oriented by first aligning the poles ($\theta = 0$ and $\theta = \pi$) with the positive and negative ends of the longest major axis of the ellipsoidal (1st-degree) spherical harmonic functions and aligning the intersection of the dateline ($\phi = 0$) and the equator ($\theta = \pi/2$) with the positive end of the shortest axis of the ellipsoid. Lastly, the RVES are oriented in object space by determining the rotations necessary to make the three main axes of the ellipsoidal spherical harmonic functions coincide with the Cartesian coordinate axes with the shortest axis of the ellipsoidal functions along the x-axis and the longest axis of the ellipsoidal functions along the z-axis. The object space rotations are then applied to all spherical harmonic function coefficients in combination with the previous operations as

$$\vec{c}_k^f = R_k^{object} \times R_k^{parameter} \times (S_k^{FOE} \times \vec{c}_k), \tag{7}$$

where $\vec{c}_k$ is the initial (following surface parameterization) spherical harmonic coefficient vector for the kth patient, S_k^{FOE}, $R_k^{parameter}$, and R_k^{object} are the scaling operator, rotation operator in parameter space, and rotation operator in object space corresponding to the kth patient, respectively, and $\vec{c}_k^f$ is the final spherical harmonic coefficient vector for this aligned individual.

2.3.4. Registration of SPHARM Parameterization:

The final approach considered to complete the correspondence with the SPHARM workflow was an approach that combines an ICP-type algorithm with a method that aligns the shapes in the space of the spherical harmonic function parameterization (in some cases referred to as the SHREC algorithm in the literature) ([39, 41]). The first step is similar to the ICP algorithm shown in Section 2.3.2, which initially aligns (i.e., rotates, translates, and scales) each shape to a pre-selected template by minimizing the distance between a selected group of landmarks prior to expansion into spherical harmonic functions. Therefore, the initially aligned k^{th} RVES (including all patients at all phases) can be shown as

$$\vec{x}_k^* = R_k^* \times (S_k^* \times \vec{x}_k) + \vec{T}_k^*, \tag{8}$$

where R_k^*, S_k^*, and T_k^* are the rotation operator, scaling operator, and translation vector, respectively. Then, each of the aligned shapes (i.e., $\vec{x}_k^*$) is parameterized and expanded to obtain the spherical harmonic function coefficients, $\vec{c}_k$. The final step rotates the spherical harmonic function coefficients using three rotation parameters, α, β, and γ, to minimize the difference between the spherical harmonic coefficient vector of each shape and the template shape to produce the final set of aligned spherical harmonic function coefficients, $\vec{c}_k^f$, as

$$\min_{\alpha, \beta, \gamma} \sqrt{\|\vec{c}_k^f(\alpha, \beta, \gamma) - \vec{c}_i\|^2}, \tag{9}$$

where

$$\vec{c}_k^f(\alpha, \beta, \gamma) = R^f(\alpha, \beta, \gamma) \times \vec{c}_k, \tag{10}$$

R^f is the rotation operator, and $\vec{c}_i$ is the spherical harmonic function coefficient vector of the selected template.

2.4. Statistical Decomposition

As stated previously, the decomposition approaches of POD and PCA are conceptually equivalent, but are differentiated herein such that POD was applied to decompose (i.e., obtain shape modes from) the continuous function RVES descriptions for the DM-POD workflow, while PCA was applied to decompose the coefficients of the spherical harmonic functions for the SPHARM workflow. Therefore, the POD approach determines the optimal set of modes

(i.e., modal shapes) $\{\vec{v}_i(\theta, \phi)\}_{i=1}^n$ in an average sense to approximate the set of mapped and aligned RVES as

$$\vec{p}_k(\theta, \phi) \approx \sum_{i=1}^n a_{ki}\vec{v}_i(\theta, \phi) + \vec{b}(\theta, \phi), \tag{11}$$

where $\vec{p}_k(\theta, \phi)$ is the kth shape or shape change function, $\vec{b}(\theta, \phi)$ is the translation function, a_{ki} are modal coefficients, and n is the total number of modes. For the present work the translation function was taken as $\vec{0}$ when analyzing the pseudo-displacement and taken as the mean shape when analyzing the shapes with the ICP alignment. Similarly, the PCA approach determines the optimal set of i.e., principle components $\{\vec{r}_i\}_{i=1}^n$ to approximate the set of spherical harmonic function coefficients for each mapped and aligned RVES as

$$\vec{c}_k \approx \sum_{i=1}^n d_{ki}\vec{r}_i + \vec{z}, \tag{12}$$

where $\vec{c}_k$ is the kth RVES spherical harmonic function coefficient vector, $\vec{z}$ is mean vector, and d_{ki} are modal coefficients. Therefore, the corresponding modal shapes $\{\vec{w}_i(\theta, \phi)\}_{i=1}^n$ can be obtained from the principal components of the spherical harmonic function coefficients as

$$\vec{w}_i(\theta, \phi) = \sum_{j=1}^{J_{max}} \left[r_{ij}^{(1)} \sin(\theta)\cos(\phi), r_{ij}^{(2)} \sin(\theta)\sin(\phi), r_{ij}^{(3)} \cos(\theta) \right]^T Y_j(\theta, \phi),$$

$$\tag{13}$$

where $\vec{r}_i$ is broken down in a consistent manner as the vector of spherical harmonic function coefficients such that $\vec{r}_i = \left[r_{i1}^{(1)}, r_{i1}^{(2)}, r_{i1}^{(3)}, r_{i2}^{(1)}, r_{i2}^{(2)}, r_{i2}^{(3)}, ... \right]^T$. See [16] for more details regarding the formulation and implementation of POD directly applied to shape analysis, and see [35] for more details regarding the formulation and implementation of PCA for shape analysis.

3. Results and Discussion

3.1. Human Cardiac Image Dataset Clinical Classification

The statistical shape analysis methods presented were applied to the discussed set of clinically obtained ECG-gated multislice cardiac computed tomography (CT) images for 13 individuals from a study on regional RV
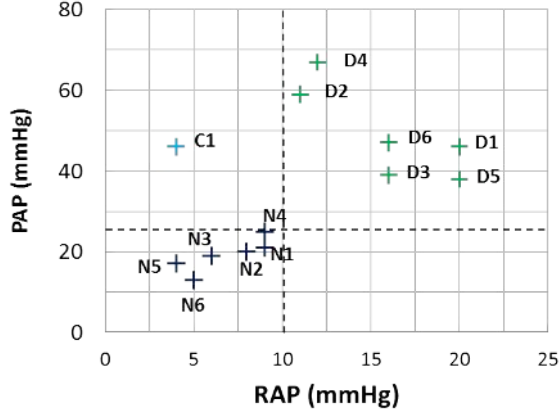
Figure 2: Hemodynamic distribution of the six non-hypertensive (marked as N1 - N6 with black cross), six hypertensive with decompensated right ventricle (RV) function (marked as D1 - D6 with green cross), and one hypertensive with compensated RV function (marked as C1 with blue cross) patients considered for this study in terms of the mean pulmonary arterial pressure (PAP) and right atrial pressure (RAP).

structural and functional adaptation to PH as previously reported in [36]. However, the 13 patients were initially clinically classified based on resting mean pulmonary arterial pressure (PAP) and right atrial pressure (RAP), with six patients grouped as "non-hypertensive" based on PAP$\leq 25mm\,Hg$ (labeled as N1-6), six patients grouped as "hypertensive with decompensated RV function" based on PAP$> 25mm\,Hg$ and RAP$> 10mm\,Hg$ (labeled as D1-6), and one patient grouped as "hypertensive with compensated RV function" based on PAP$> 25mm\,Hg$ and RAP$< 10mm\,Hg$ (labeled as C1). Fig. 2 shows the distributions of PAP and RAP for the 13 patients within the dataset. In all cases, patients with RAP$> 10mm\,Hg$ also had a cardiac index $< 2.0L/min/m^2$. An important note is that all patients within the study (even those classified as "non-hypertensive") are symptomatic, and therefore, not an average healthy individual. To provide an additional clinical metric relating to RV function, Fig. 3 shows the volume ejection fraction in comparison to one reported normal cutoff [42] for each of the 13 patients, although it should be noted that currently there is no clinically agreed upon value range for "normal" RV ejection fraction.

3.2. Mapping and Alignment

Fig. 4 shows the initial orientation (i.e., the orientation of the RVES after segmentation, but prior to any alignment) of a representative set of six segmented and smoothed RVES shapes at the ED phase, as well as the re-
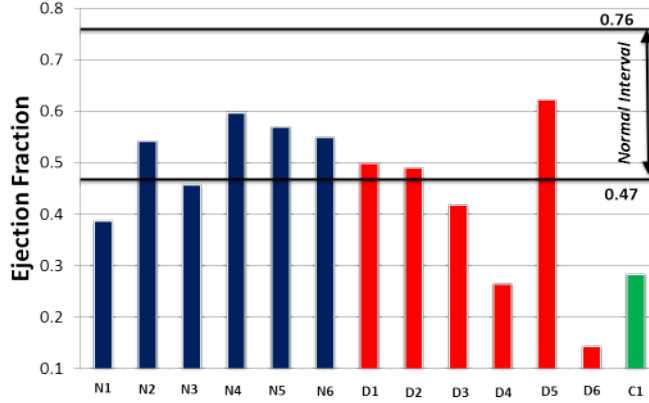
Figure 3: Ejection fraction of the six non-hypertensive (N1 - N6), six hypertensive with decompensated right ventricle (RV) function (D1 - D6), and one hypertensive with compensated RV function (C1) patients considered for this study (note that there is some question over the appropriate "normal interval" of EF, and the value shown here is solely to provide a relative perspective for the patient set).

sults of the mapping to spherical coordinates and orientations of each RVES following the various parameterization and alignment methods of each work-flow (note that the pseudo-displacement alignment results are not shown since this approach is the only method not routed in traditional registration, and therefore not directly comparable in this manner to the other strategies). Note that the mapping results are displayed through the color contours, such that the colors correspond to values of the mapping variables (i.e., the spherical coordinates θ and ϕ) as shown in Fig. 4. In addition, for the SPHARM workflow two additional trials were performed (labeled with "Updated"), in which the orientations of the RVES were first manually adjusted according to the anatomical references (i.e., the RVES were manually rotated to place the pulmonary valve, apex, septum, and free wall in a similar posture throughout the population) and then the two SPHARM alignment methods in combination with the parameterization algorithm were applied again.

Overall, the alignment results for the ICP algorithm within the DM-POD framework appeared to orient all of the RVES such that the various anatomical regions that can be identified (e.g., the pulmonary outflow track, the tricuspid valve, the apex, the free wall, and the septum) were in consistently similar relative positions. The FOE and SHREC algorithms from the SPHARM workflow oriented the majority of the RVES with a similar amount of anatomical consistency in comparison to the ICP algorithm in the
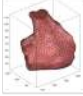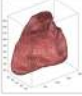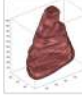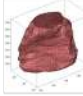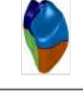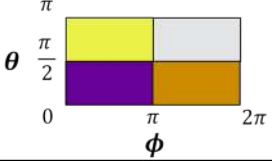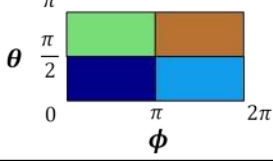
Figure 4: Initial orientation of a representative set of six segmented and smoothed right ventricle endo-cardial surface (RVES) shapes at the end diastole (ED) phase of the cardiac cycle, including two non-hypertensive patients (N3 & N5), three hypertensive with decompensated right ventricle (RV) function patients (D1, D5, & D6), and one hypertensive with compensated RV function patient (C1), as well as the results of the mapping to spherical coordinates (color contours) and orientations of each RVES following the two step harmonic mapping and the iterative closest point (ICP) alignment of the DM-POD workflow, and the harmonic mapping followed by the control of area and length distortions (CALD) algorithm and the first order ellipsoid (FOE) or the SHREC alignment of the SPHARM workflow. Additionally, for the SPHARM workflow the two updated alignment trials are shown (labeled with "Updated"), where the orientation of the RVES were manually adjusted according to the anatomical references and then the two SPHARM alignment algorithms in combination with the parameterization algorithm were applied again.

DM-POD workflow. However, some of the registration results for the FOE and SHREC algorithms were far less anatomically consistent compared to the ICP algorithm. For example, after applying the FOE algorithm the free wall for patient $N3$ was facing outward rather than to the right, as was the rest of the population, and the pulmonary valve for patient $D5$ was pointing outward rather than toward the top. Furthermore, after applying the SHREC algorithm the orientations of nearly all of the anatomical features for patient $N3$ were in significantly different positions compared to the rest of the population, but generally the SHREC algorithm appeared to produce orientations that were anatomically similar more consistently throughout the population than the FOE algorithm. This lack of anatomical consistency for the FOE and SHREC algorithms is not necessarily unexpected though, since the objective driving the registration process for those algorithms is based more on shape features (i.e., the spherical harmonic expansion) than anatomical features, particularly the FOE algorithm, in contrast to the entirely anatomical reference-based ICP algorithm used in the DM-POD workflow. One additional reason for the inconsistency in the orientation of the anatomical features in the results from the FOE and SHREC algorithms is that both algorithms depend significantly upon the initial orientation of the surfaces. Thus, if the surfaces are initially substantially different in the anatomical orientation they are more likely to remain different in the anatomical orientation following FOE or SHREC alignment. As such, the "Updated" FOE and SHREC results, in which the initial RVES orientation was manually set to be more anatomically consistent across the population, show some increase in the anatomical consistency across the population for the final oriented shapes. **For the Updated SHREC results all of the RVES could be considered to have similar relative positioning of the anatomical features. In contrast, for the FOE results there were still some RVES that had substantially different orientations in terms of the anatomical references (e.g., $D5$), and therefore, this analysis approach was not considered for further analysis (i.e., only the updated SHREC results are considered further herein).** In general, the results for the spherical coordinate mapping (i.e., color contours) followed a similar pattern to the results for the RVES orientation, particularly for the SPHARM workflow techniques, which have a direct connection between the mapping and alignment results in the processing steps. The DM-POD workflow produced mappings that assigned values for the spherical coordinate to the various anatomical regions that were relatively similar across the population, while
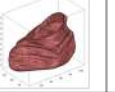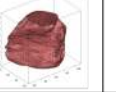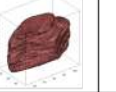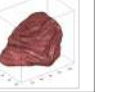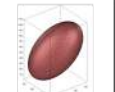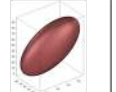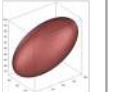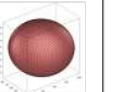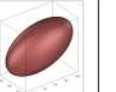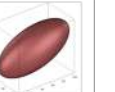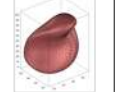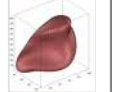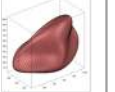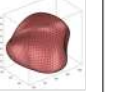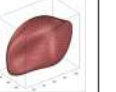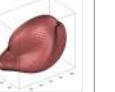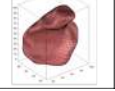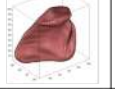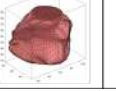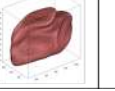
Patient#	N3	N5	D1	D5	D6	C1
Manually Rotated DM-POD						
SPHARM						
Degree 1						
Degree 5						
Degree 15						

Figure 5: A representative set of six segmented and smoothed right ventricle endocardial surface (RVES) shapes at the end diastole (ED) phase of the cardiac cycle, including two non-hypertensive patients (N3 & N5), three hypertensive with decompensated right ventricle (RV) function patients (D1, D5, & D6), and one hypertensive with compensated RV function patient (C1), manually rotated to be anatomically consistent, and the expansion of each RVES onto a collection of spherical harmonic functions after parameterization (as used within the SPHARM workflow), for spherical harmonic function bases of degree 1 (4 basis functions), degree 5 (36 basis functions), and degree 15 (256 basis functions) (with orientation maintained consistently).

the SPHARM workflow had some amount of anatomical consistency, but showed substantially more variation in the spherical coordinate values for the various anatomical regions for some members of the population.

To further understand the nature of the shape descriptions, Fig. 5 shows the expansion of the representative set of RVES onto sets of spherical harmonic functions of varying basis order, as used in the SPHARM workflow, in comparison to the complete (i.e., non-expanded) description, as utilized in the DM-POD workflow. The first degree expansion is an ellipsoid, and this is the component that is primarily used for the FOE alignment. As such, the relatively large variation in the shape of this ellipsoid component can be understood as the core reason why the FOE alignment method produced substantial variations in the relative orientation of the anatomical features of the RVES (shown in Fig. 4). Regarding the representation, as would be expected, as the number of spherical harmonic basis functions included in the representation increases, the number of details of the RVES preserved by the representation also increases. What is more interesting is that a relatively large number of spherical harmonic functions are required to clearly represent

the RVES. At degree 5, which equates to a total of 36 basis functions, the outline of the RVES begins to emerge, but details of some structures such as the pulmonary valve region and the papillary muscles along the free wall and septum are missing. Even at degree 15, which equates to a total of 256 basis functions, the majority of the details of the original RVES are recovered, but some fine-scale details can still be seen as missing in comparison to the original surfaces. While this expansion onto the spherical harmonic function basis may result in what could be considered as a loss of information, the expansion may alternately be viewed as a filtering process to remove features that could be contaminated by noise.

3.3. Statistical Decomposition

POD (for the DM-POD workflow) and PCA (for the SPHARM workflow) were applied to decompose the respective sets of parameterized and aligned RVES. However, note that while both the ICP and pseudo-displacement results were decomposed with POD for the DM-POD workflow, for brevity, the PCA decomposition in the SPHARM workflow was considered only for the parameterization and alignment results of the Updated SHREC algorithm, since the Updated SHREC results were the most similar to the ICP results for the DM-POD workflow with regards to the anatomical orientations. Additionally, four different approaches for using the available information within the cardiac cycle (i.e., phases) were considered: (1) analyzing the RVES at the single ED phase for each patient, (2) analyzing the RVES at the single ES phase, (3) analyzing the RVES at both the ED and ES phases, and (4) analyzing the RVES at all nine available phases for each patient. As would be expected, the pseudo-displacement method was only applied to approaches (3) and (4), in which the pseudo-displacement functions were calculated with the RVES at ED as the reference phase (i.e., all other phases were subtracted from the ED phase to produce the pseudo-displacement functions).

As an example of the appearance of the modal shapes that can be obtained from the decomposition methods Fig. 6 shows representations of the 3D modal shapes obtained by applying POD to the ICP results for the DM-POD workflow and applying PCA to the SHREC results for the SPHARM workflow to analyze only the ED phase of all 13 patients. More specifically, Fig. 6 shows the mean shape (i.e., the average shape of the RVES at ED over the 13 patients) in comparison to the mean shape combined with the specified modal shape multiplied by ± 1 or 2 standard deviations σ_i of the corresponding i^{th} modal coefficient value across the set of 13 patients. Note

that the modes produced by both workflows are ranked by their relative contribution to the representation of the set of 13 patients, such that mode 1 has the largest contribution to the shape over the set of patients, followed by mode 2, and so on. As can be seen, there were distinct differences between the modal shapes produced by each approach within each framework. For example, mode 3 obtained from the DM-POD workflow in Fig. 6 shows a concentrated shape variation directly below the outflow tract, while mode 3 obtained from the SPHARM workflow has no such specific regional variation, and there is actually no other mode within the set produced by the SPHARM workflow that could be considered similar in appearance to mode 3 from the DM-POD workflow. However, there is not necessarily any method to assess which modal shape set is preferred, particularly since the physiological relevance of the modes is limited in that each is strictly one statistical representation of the shape sets and subject to the mathematical constraints of the decomposition, such as orthogonality.

Since there is limited physical interpretation of these statistically generated modal shapes, it is often more useful to analyze how the various modes contribute to the representation of the shape datasets to understand the relative compactness of the modal representations, the information content within each mode, and how much variation there is in this shape information across the datasets. To understand these modal contributions Fig. 7 shows the cumulative modal energy for both the POD and PCA results for each of the four groupings of the cardiac phase data. For the ith mode the cumulative modal energy was calculated as

$$C_i = \frac{\sum_{j=1}^{i} \lambda_j}{\sum_{k=1}^{n} \lambda_k}, \tag{14}$$

where λ_k is the eigenvalue obtained through the POD/PCA process corresponding to the kth mode and n is the total number of modes obtained by the decomposition. For all trials, the cumulative energy curve for the modes obtained from the DM-POD approach can be seen to be considerably steeper than the energy curve for modes obtained from the SPHARM approach, both when analyzing the shape (ICP results) and the change in shape (pseudo-displacement results). Thus, it can be inferred that with an equivalent number of modes the DM-POD results preserve more information within the population (i.e., are a more compact representation) than the SPHARM results. In other words, in order to retain the same amount of

	$- 2\sigma_i$	$- \sigma_i$	Mean	$+ \sigma_i$	$+ 2\sigma_i$
Mode1					
Mode2					
Mode3					

(a)

	$- 2\sigma_i$	$- \sigma_i$	Mean	$+ \sigma_i$	$+ 2\sigma_i$
Mode1					
Mode2					
Mode3					

(b)

Figure 6: The mean shape and plus or minus one and two standard deviations ($\pm\sigma_i$ and $\pm2\sigma_i$) of each of the first three modal coefficient values multiplied with the corresponding mode shape and added to the mean shape for analysis of the dataset of 13 patient's right ventricle endocardial surface shapes at the end diastole phase in the cardiac cycle with (a) the DM-POD workflow with ICP alignment and (b) the SPHARM workflow with the "Updated" SHREC alignment.

information the SPHARM approach needs to utilize more modes than the DM-POD approach. However, there was minimal variation in the energy distribution for different groupings of the cardiac phase information or comparing the pseudo-displacement results to the ICP results in the DM-POD workflow. Therefore, the results would indicate that the specific workflow had substantially more influence on the compactness of the modal representations than the particular cardiac phase grouping or the representation as shape change rather than shape.

3.4. Clustering

The last set of tests was intended to analyze the applicability and differences of the statistical shape analysis methods towards the ultimate goal of identifying and classifying shape-based patterns within patient sets. Therefore, the final set of tests considered the variations in the modal shape components across the patient set for the various analysis methods and how these modal components could potentially be used to separate the patient set into various groupings (i.e., clusters).

First, a basic K-means clustering algorithm ([43]) was applied to group the 13 patients within the set based on the modal coefficients extracted for each patient through the DM-POD workflow with the ICP (shape) and pseudo-displacement (shape change) strategies and the SPHARM workflow with the Updated SHREC (shape) technique for all four groupings of the cardiac phases considered (as were also considered in Section 3.3). The number of modes used to represent each patient (m) were selected such that at least 99% of the cumulative energy was captured for the set respectively for each approach (based on the eigenvalue analysis discussed previously), and each patient was then described for the clustering process by a vector of the individual relative modal energy percentages (as was used in [16]), with the components of this vector calculated as

$$M_i = \frac{\sum_{k=1}^{n} a_{ki}^2}{\sum_{j=1}^{N} \sum_{p=1}^{n} a_{pj}^2} \times 100\%, \quad \text{for} \quad i = 1, 2, ..., m, \tag{15}$$

where a_{ki} is the modal coefficient for the given patient corresponding to the ith mode included in the vector and the kth cardiac phase, N is the total number of modes obtained from the decomposition process of the set of 13 individuals,

(a)

(b)

(c)
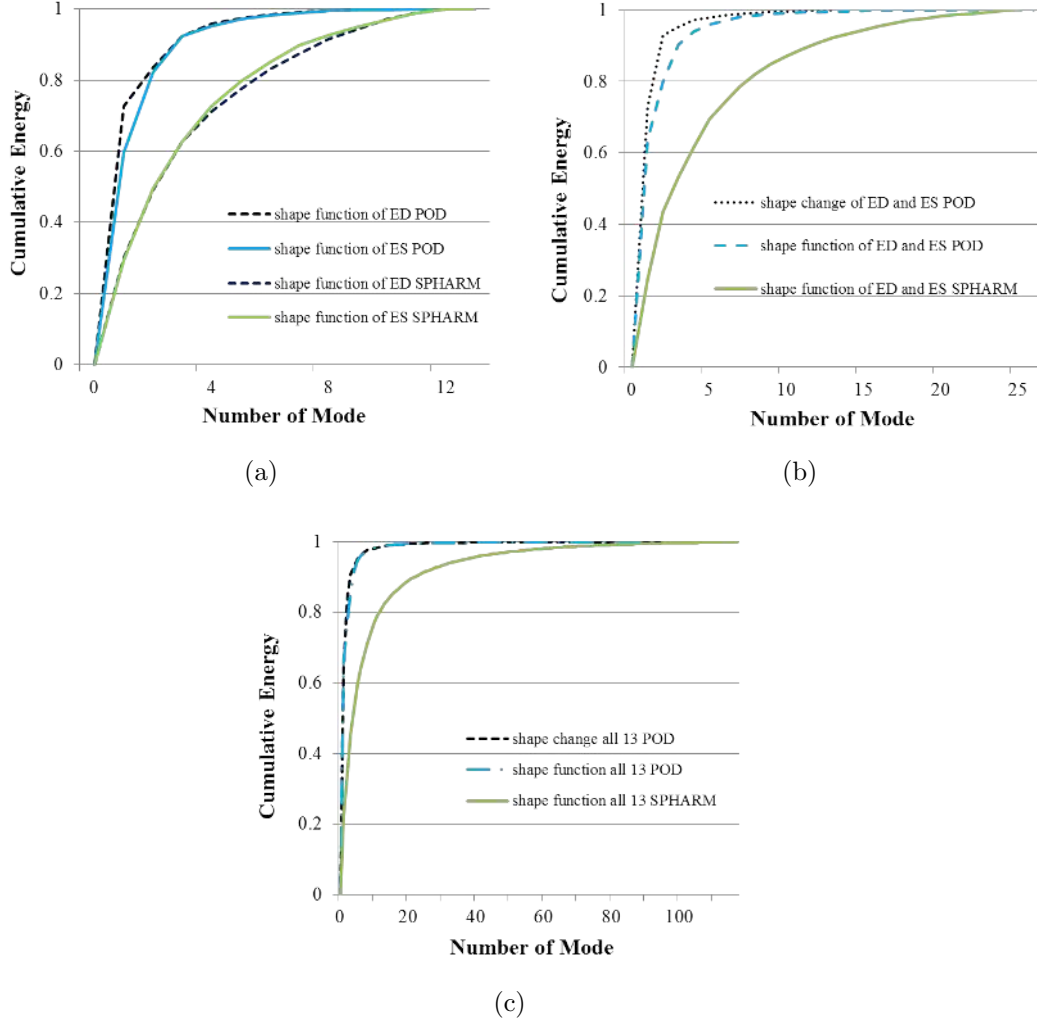
Figure 7: The cumulative modal energy for the POD and ICA modes obtained for the 13-patient dataset from analysis of (a) the end diastole (ED) and end systole (ES) phases in the cardiac cycle alone with the DM-POD workflow with ICP alignment and the SPHARM workflow with the "Updated" SHREC alignment, (b) the ED and ES phases combined with the DM-POD workflow with the pseudo-displacement (PD) alignment (subtracting the ED phase from the ES phase), the DM-POD workflow with ICP alignment, and the SPHARM workflow with the "Updated" SHREC alignment, and (c) all available phases with the DM-POD workflow with the PD alignment (subtracting the ED phase from all other phases), the DM-POD workflow with ICP alignment, and the SPHARM workflow with the "Updated" SHREC alignment.

26
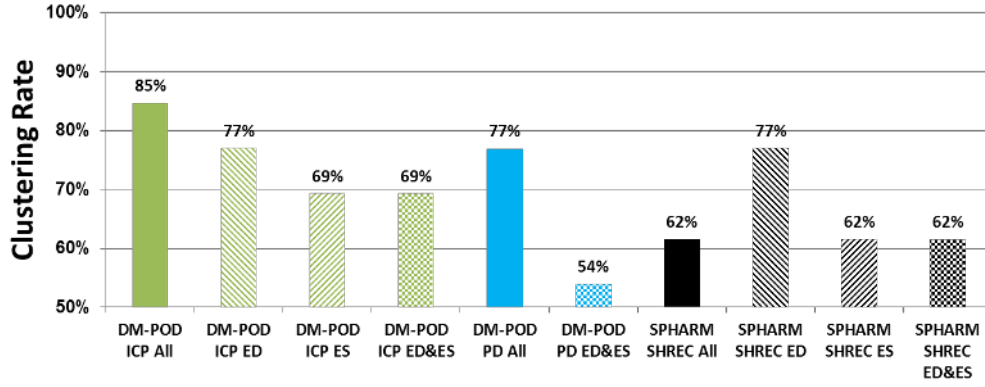
Figure 8: Percentage (i.e., Clustering Rate) of patients from the 13-patient dataset that were grouped by K-means clustering (assuming two classes) with the majority of patients in the same classification (hypertensive or non-hypertensive) based on the feature vector of the individual relative modal energy percentages from the DM-POD workflow analysis with ICP alignment of all available phases in the cardiac cycle, the end diastole (ED) phase alone, the end systole (ES) phase alone, and the ED and ES phases combined, the DM-POD workflow analysis with the pseudo-displacement (PD) alignment (subtracting the ED phase from all other phases) of all available phases and the ED and ES phases combined, and SPHARM workflow analysis with the "Updated" SHREC alignment of all available phases, the ED phase alone, the ES phase alone, and the ED and ES phases combined.

and n is the number of phases in the cardiac cycle used for the particular analysis case. To assess how the modal representations would group the patient set, not only with respect to each other, but also in comparison to the most basic clinical metrics that are used to classify RV function, the number of groupings was arbitrarily set to two and the groupings were compared with the clinical classification of "hypertensive" and "non-hypertensive" defined in Section 3.1. As such, Fig. 8 shows the percentage of the patients that were grouped by the K-means clustering with a majority of patients in the same classification (hypertensive or non-hypertensive) for each of the analysis approaches considered. There was a substantial variation in the rate at which the various workflows and analysis methods grouped the patients in agreement with the hypertensive/non-hypertensive classification, and thus, substantial variation in the way in which the methods grouped the patients in general. The DM-POD workflow analysis of all cardiac phases with the ICP alignment showed the highest rate of agreement with the clinical classification and the DM-POD workflow analysis of the ED and ES phases with the pseudo-displacement alignment produced the lowest rate of agreement, yet on average the results of the DM-POD workflow grouped the patients more consistently in agreement with the clinical classification than the SPHARM workflow. The results could be further interpreted to indicate that the shape

27

of the ED phase and one more more of the intermediate phases in the cardiac cycle is more strongly correlated with the state of hypertension, while the shape of the ES phase is related to other aspects of RV function.

To explore the nature of the potential clustering capabilities of the statistical shape analysis methods further hierarchical clustering tests were performed on the two analysis techniques (one from each workflow) that had the strongest agreement with the hypertension classification in the K-means clustering results: the DM-POD workflow analysis of all cardiac phases with the ICP algorithm and the SPHARM workflow analysis of the ED phase with the Updated SHREC algorithm. Note that the choice to compare the workflow-cardiac phase combinations based on agreement with the hypertension classification as a representative example was arbitrary and done for the purpose of brevity. To also provide an alternate comparison of standard clinically measurable RV function an additional feature vector was created for each patient consisting of the pulmonary arterial pressure, the right atrial pressure, and the ejection fraction, with all values normalized with respect to the largest respective value in the patient set. Fig. 9 shows the clustering results after applying hierarchical clustering ([43]) to the DM-POD and SPHARM relative modal energy feature vectors, as described above, as well as the clinical pressure-volume feature vector, with the vertical lines in the figure indicating the relative distance in the feature space between the patient groups connected by the horizontal lines. As would be expected, the clinical pressure-volume features clustered all non-hypertensive patients in one group with a relatively large distance from this group to the hypertensive patient group. However, it is interesting to observe that the patient with compensated RV function was clustered considerably closer in the clinical feature space to two of the patients with decompensated RV function than those three are to the rest of the hypertensive patients with decompensated RV function and all of the hypertensive patients were clustered relatively far from each other in comparison to the non-hypertensive patients, further highlighting the wide spectrum of patient hemodynamic states and the complexity of the affects of PH on RV function. The results from the DM-POD workflow led to clustering all of the non-hypertensive patients within one relatively compact group, but also included two of the decompensated hypertensive patients in the same grouping, while having a diverse spectrum, in a similar way as the clinical features, for the remaining decompensated and compensated hypertensive patients. Alternatively, the hierarchical clustering results for the SPHARM workflow placed one decompensated hypertensive

28
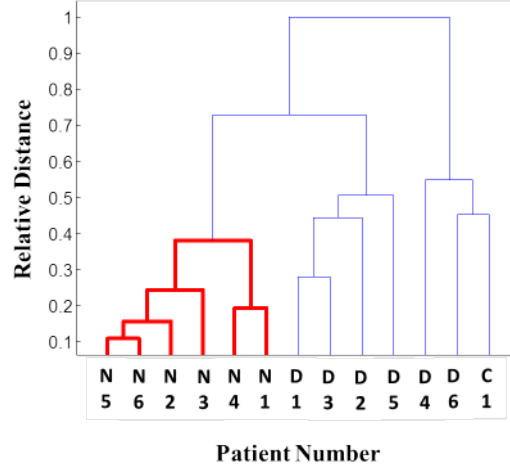
(a)
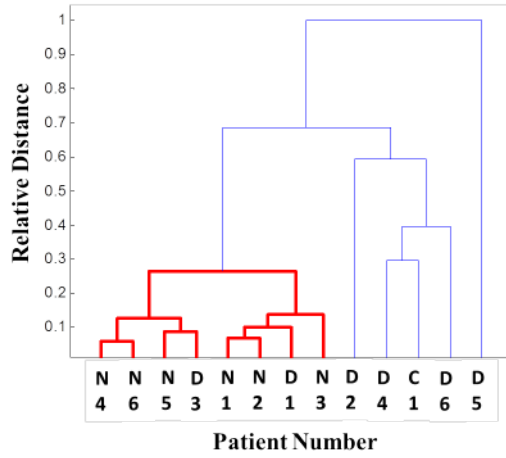
(b)
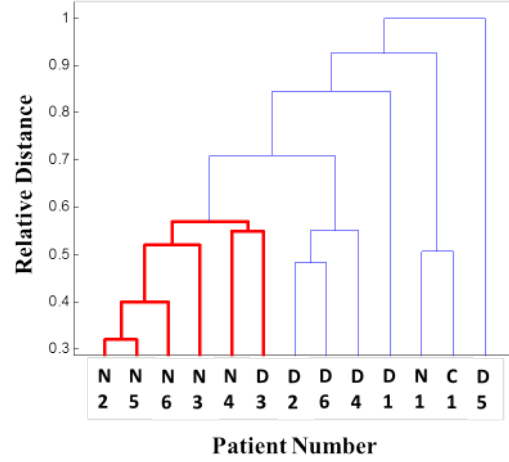
(c)

Figure 9: Hierarchical clustering results (relative distance between feature vectors in the set) of the 13-patient dataset, including the 6 non-hypertensive individuals (N1 - N6), the 6 hypertensive with decompensated right ventricle (RV) function individuals (D1 - D6), and the 1 hypertensive with compensated RV function individual (C1), for the (a) clinical normalized pressure-volume feature vector, (b) individual relative modal energy percentage feature vector from the results of the DM-POD workflow with ICP alignment analysis of all available cardiac phases, and (c) individual relative modal energy percentage feature vector from the results of the SPHARM workflow with the "Updated" SHREC alignment analysis of only the end diastole cardiac phase.

individual in a group with five other non-hypertensive individuals, while placing one non-hypertensive individual within the other group of the remaining hypertensive individuals. Yet, the overall distribution of the patients for the SPHARM workflow clustering is substantially more widespread than the two other approaches, with only relatively small groupings of patients (i.e., two or three) being placed relatively close together. However, it is generally impossible to say whether one approach or another is a "better" indicator of RV function, relating to PH or otherwise in this preliminary clustering analysis, but rather the results are an indication that these analysis approaches relate differently to the state of the RV (with pressure being one aspect of the state of the RV), and that there is value in exploring the various strategies in the future to identify the workflow components and the cardiac phase information that could potentially provide the necessary information to classify functional changes throughout the course of a disease such as PH.

4. Conclusions

Two different statistical shape analysis workflows to assess human RV function were discussed and analyzed, including an approach that directly applies POD to harmonically mapped surfaces, and an approach that also harmonically maps the surfaces, but then projects the surfaces onto spherical harmonic functions prior to further analysis. Each step of both workflows, including the surface representation, parameterization, registration, and statistical decomposition, were elaborated upon, and the techniques were tested with a collection of human RVES. The DM-POD workflow appeared to provide surface mappings and alignments that were more anatomically consistent than the SPHARM workflow with respect to observable regions of the RV, such as the septum, free wall, pulmonary and tricuspid valves, and the apex. Additionally, the two workflows were shown to extract shape-related features that are distinctly different from one another, while the pattern analysis (shown in terms of clustering) of the patient set is closely related to both the various aspects of the workflows and the specific cardiac phase information utilized for the analysis. On average, the DM-POD workflow clustered the patient set in closer agreement with the standard clinical hemodynamic metrics in comparison to the SPHARM workflow, while the ED and other intermediate phases of the cardiac cycle produced shape features that were relatively correlated with the state of hypertension, whereas the shape of the ES phase is related to other aspects of RV function. Overall, both the

DM-POD and SPHARM workflows where shown to produce features that relate distinctly to the state of the RV, and the observations herein provide a foundation for future work to determine the specific statistical shape analysis techniques and cardiac phase components to provide the necessary information to effectively classify functional changes in the human RV.

5. Acknowledgment

References

[1] J. N. Cohn, R. Ferrari, N. Sharpe, Cardiac remodelingconcepts and clinical implications: a consensus paper from an international forum on cardiac remodeling, Journal of the American College of Cardiology 35 (3) (2000) 569–582.

[2] S. F. Nagueh, C. P. Appleton, T. C. e. a. Gillebert, Recommendations for the evaluation of left ventricular diastolic function by echocardiography., Journal of the American Society of Echocardiography official publication of the American Society of Echocardiography 10 (2) (2009) 1–9.

[3] G. Simonneau, I. M. Robbins, M. Beghetti, R. N. Channick, M. Delcroix, C. P. Denton, C. G. Elliott, S. P. Gaine, M. T. Gladwin, Z.-C. Jing, et al., Updated clinical classification of pulmonary hypertension., Journal of the American College of Cardiology 54 (1 Suppl) (2009) S43–S54.

[4] C. Apitz, G. D. Webb, A. N. Redington, Tetralogy of fallot, THE LANCET 374 (24-30) (2009) 1462–1471.

[5] A. Hyduk, J. B. Croft, C. Ayala, K. Zheng, Z.-J. Zheng, G. A. Mensah, Pulmonary hypertension surveillance–united states, 1980-2002., MMWR Surveillance summaries Morbidity and mortality weekly report Surveillance summaries CDC 54 (5) (2005) 1–28.

[6] M. A. Simon, Assessment and treatment of right ventricular failure, Nature Reviews Cardiologydoi:10.1038/nrcardio.2013.12.

[7] K. Doi, Computer-aided diagnosis in medical imaging: historical review, current status and future potential., Computerized medical imaging and graphics the official journal of the Computerized Medical Imaging Society 31 (4-5) (2007) 198–211.

[8] M. B. Stegmann, D. D. Gomez, R. P. Plads, D. K. Lyngby, A brief introduction to statistical shape analysis, Analysis I (March) (2002) 1–15.

[9] D. Adams, F. J. Rohlf, D. Slice, Geometric morphometrics: Ten years of progress following the revolution, Italian Journal of Zoology 71 (1) (2004) 5–16.

[10] A. Srivastava, S. H. Joshi, W. Mio, X. Liu, Statistical shape analysis: clustering, learning, and testing., IEEE Transactions on Pattern Analysis and Machine Intelligence 27 (4) (2005) 590–602.

[11] J. G. Bosch, F. Nijland, S. C. Mitchell, B. P. F. Lelieveldt, O. Kamp, J. H. C. Reiber, M. Sonka, Computer-aided diagnosis via model-based shape analysis: automated classification of wall motion abnormalities in echocardiograms., Academic Radiology 12 (3) (2005) 358–367.

[12] S. H. Kim, J.-M. Lee, H.-P. Kim, D. P. Jang, Y.-W. Shin, T. H. Ha, J.-J. Kim, I. Y. Kim, J. S. Kwon, S. I. Kim, Asymmetry analysis of deformable hippocampal model using the principal component in schizophrenia., Human Brain Mapping 25 (4) (2005) 361–369.

[13] M. Styner, J. A. Lieberman, D. Pantazis, G. Gerig, Boundary and medial shape analysis of the hippocampus in schizophrenia., Medical Image Analysis 8 (3) (2004) 197–203.

[14] T. Mansi, I. Voigt, B. Leonardi, X. Pennec, S. Durrleman, M. Sermesant, H. Delingette, A. M. Taylor, Y. Boudjemline, G. Pongiglione, et al., A statistical model for quantification and prediction of cardiac remodelling: Application to tetralogy of fallot, IEEE Transactions on Medical Imaging 30 (9) (2011) 1605–1616.

[15] H. Zhang, A. Wahle, R. K. Johnson, T. D. Scholz, M. Sonka, 4-d cardiac mr image analysis: left and right ventricular morphology and function., IEEE Transactions on Medical Imaging 29 (2) (2010) 350–364.

[16] J. Wu, Y. Wang, M. Simon, J. Brigham, A new approach to kinematic feature extraction from the human right ventricle for classification of hypertension: a feasibility study, Physics in Medicine and Biology 40 (7) (2012) 2005–2010.

[17] T. Heimann, H.-P. Meinzer, Statistical shape models for 3d medical image segmentation: a review., Medical Image Analysis 13 (4) (2009) 543–563.

[18] S. A. Meda, B. Narayanan, J. Liu, N. I. Perrone-Bizzozero, M. C. Stevens, V. D. Calhoun, D. C. Glahn, L. Shen, S. L. Risacher, A. J. Saykin, et al., A large scale multivariate parallel ica method reveals novel imaging-genetic relationships for alzheimers disease in the adni cohort., NeuroImage 60 (3) (2012) 1608–21.

[19] P. M. Thompson, K. M. Hayashi, G. I. de Zubicaray, A. L. Janke, S. E. Rose, J. Semple, M. S. Hong, D. H. Herman, D. Gravano, D. M. Doddrell, A. W. Toga, Mapping hippocampal and ventricular change in alzheimer disease, NeuroImage 22 (4) (2004) 1754 – 1766. doi:DOI: 10.1016/j.neuroimage.2004.03.040.

[20] M. S. Floater, K. Hormann, Surface parameterization : a tutorial and survey, Advances in multiresolution for geometric modelling 1 (c) (2005) 157–186.

[21] T. F. Cootes, C. J. Taylor, Statistical models of appearance for computer vision, World Wide Web Publication February.

[22] M. Styner, I. Oguz, S. Xu, C. Brechbhler, D. Pantazis, J. J. Levitt, M. E. Shenton, G. Gerig, Framework for the statistical shape analysis of brain structures using spharm-pdm., The insight journal (1071) (2006) 242–250.

[23] L. Ferrarini, H. Olofsen, W. M. Palm, M. A. Van Buchem, J. H. C. Reiber, F. Admiraal-Behloul, Games: growing and adaptive meshes for fully automatic shape modeling and analysis., Medical Image Analysis 11 (3) (2007) 302–314.

[24] G. Gerig, M. Styner, D. Jones, D. Weinberger, J. Lieberman, Shape analysis of brain ventricles using spharm, Proceedings IEEE Workshop

on Mathematical Methods in Biomedical Image Analysis MMBIA 2001 (2001) 171–178.

[25] P. Yu, P. E. Grant, Y. Qi, X. Han, F. Sgonne, R. Pienaar, E. Busa, J. Pacheco, N. Makris, R. L. Buckner, et al., Cortical surface shape analysis based on spherical wavelets, IEEE Transactions on Medical Imaging 26 (4) (2007) 582–597.

[26] M. Styner, G. Gerig, J. Lieberman, D. Jones, D. Weinberger, Statistical shape analysis of neuroanatomical structures based on medial models., Medical Image Analysis 7 (3) (2003) 207–220.

[27] D. Meier, E. Fisher, Parameter space warping: shape-based correspondence between morphologically different objects, IEEE Transactions on Medical Imaging 21 (1) (2002) 31–47.

[28] A. Sarkar, R. J. Santiago, R. Smith, A. Kassaee, Comparison of manual vs. automated multimodality (ct-mri) image registration for brain tumors., Medical dosimetry official journal of the American Association of Medical Dosimetrists 30 (1) (2005) 20–24.

[29] D. Chetverikov, D. Stepanov, P. Krsek, Robust euclidean alignment of 3d point sets: the trimmed iterative closest point algorithm, Image and Vision Computing 23 (3) (2005) 299–309.

[30] C. Goodall, Procrustes methods in the statistical analysis of shape, Journal of the Royal Statistical Society Series B Methodological 53 (2) (1991) 285–339.

[31] F. Wiesmann, J. Ruff, S. Engelhardt, L. Hein, C. Dienesch, A. Leupold, R. Illinger, A. Frydrychowicz, K. H. Hiller, E. Rommel, et al., Dobutamine-stress magnetic resonance microimaging in mice : acute changes of cardiac geometry and function in normal and failing murine hearts., Circulation Research 88 (6) (2001) 563–569.

[32] A. F. Frangi, D. Rueckert, J. A. Schnabel, W. J. Niessen, Automatic construction of multiple-object three-dimensional statistical shape models: application to cardiac modeling., IEEE Transactions on Medical Imaging 21 (9) (2002) 1151–1166.

[33] H. Huang, L. Shen, R. Zhang, F. Makedon, B. Hettleman, J. Pearlman, Cardiac motion analysis to improve pacing site selection in crt., Academic Radiology 13 (9) (2006) 1124–1134.

[34] A. Andreopoulos, J. K. Tsotsos, Efficient and generalizable statistical models of shape and appearance for analysis of cardiac mri., Medical Image Analysis 12 (3) (2008) 335–357.

[35] L. Shen, H. Farid, M. A. McPeek, Modeling three-dimensional morphological structures using spherical harmonics., Evolution: International Journal of Organic Evolution 63 (4) (2009) 1003–1016.

[36] M. A. Simon, C. Deible, M. A. Mathier, J. Lacomis, O. Goitein, S. G. Shroff, M. R. Pinsky, Phenotyping the right ventricle in patients with pulmonary hypertension., Clinical and translational science 2 (4) (2009) 294–299.

[37] C. Brechbuhler, G. Gerig, O. Kobler, Parameterization of closed surfaces for 3d shape description, Computer Vision and Image Understanding 61 (1995) 154–170.

[38] J. Wu, Y. Wang, M. Simon, M. Sacks, J. Brigham, A new computational framework for anatomically consistent 3d statistic shape analysis with clinical imaging applications, Computer Methods in Biomechanics and Biomedical Engineering: Imaging and Visualization 1 (2013) 13–27.

[39] L. Shen, F. Makedon, Spherical mapping for processing of 3d closed surfaces, Image and Vision Computing 24 (7) (2006) 743–761.

[40] R. Estpar, A. Brun, Robust generalized total least squares, Medical Image Computing and Computer-Assisted Intervention - MICCAI 2004 (2004) 234–241.

[41] L. Shen, H. Huang, F. Makedon, A. Saykin, Efficient registration of 3d spharm surfaces, Fourth Canadian Conference on Computer and Robot Vision (2007) 81–88.

[42] A. F. Frangi, W. J. Niessen, M. A. Viergever, Three-dimensional modeling for functional analysis of cardiac images: a review., IEEE Transactions on Medical Imaging 20 (1) (2001) 2–25.

[43] R. O. Duda, P. E. Hart, D. G. Stork, Pattern Classification, 2nd Edition, Wiley, New York, 2001.